Available online at www.sciencedirect.com

SCIENCE DIRECT®

Tectonophysics 385 (2004) 137–158

TECTONOPHYSICS

www.elsevier.com/locate/tecto

Geophysical images of the creeping segment of the San Andreas fault: implications for the role of crustal fluids in the earthquake process

P.A. Bedrosian[a,*], M.J. Unsworth[b], G.D. Egbert[c], C.H. Thurber[d]

[a] *Department of Earth and Space Sciences, University of Washington, Seattle, WA 98195, USA*
[b] *Department of Physics, University of Alberta, Edmonton, Alberta, Canada T6G 2J1*
[c] *College of Ocean and Atmospheric Sciences, Oregon State University, Corvallis, OR 97331, USA*
[d] *Department of Geology and Geophysics, University of Wisconsin, Madison, WI 56706, USA*

Received 17 September 2002; received in revised form 15 July 2003; accepted 10 February 2004
Available online 2 July 2004

Abstract

High-resolution magnetotelluric (MT) studies of the San Andreas fault (SAF) near Hollister, CA have imaged a zone of high fluid content flanking the San Andreas fault and extending to midcrustal depths. This zone, extending northeastward to the Calaveras fault, is imaged as several focused regions of high conductivity, believed to be the expression of tectonically bound fluid pockets separated by northeast dipping, impermeable fault seals. Furthermore, the spatial relationship between this zone and local seismicity suggests that where present, fluids inhibit seismicity within the upper crust (0–4 km). The correlation of coincident seismic and electromagnetic tomography models is used to sharply delineate geologic and tectonic boundaries. These studies show that the San Andreas fault plane is vertical below 2 km depth, bounding the southwest edge of the imaged fault-zone conductor (FZC). Thus, in the region of study, the San Andreas fault acts both as a conduit for along-strike fluid flow and a barrier for fluid flow across the fault. Combined with previous work, these results suggest that the geologic setting of the San Andreas fault gives rise to the observed distribution of fluids in and surrounding the fault, as well as the observed along-strike variation in seismicity.

Keywords: San Andreas fault; Calaveras fault; Magnetotellurics; Hollister; Seismic tomography

1. Introduction

Large strike-slip faults such as the San Andreas fault (SAF) and North Anatolian fault have generated some of the most destructive earthquakes of the last century. A range of geological and geophysical studies in the last 20 years have greatly improved our understanding of the earthquake rupture process. These faults often show significant spatial and temporal variations in seismic behavior. For example, the San Andreas fault is characterized by a creeping central segment, with locked segments to the north and south, each having ruptured just once during the historical record (Allen,

* Corresponding author. Now at: GeoForschungsZentrum—Potsdam, Telegrafenberg, Potsdam D-14473, Germany. Tel.: +49-331-288-1258; fax: +49-331-288-1235.
E-mail address: bedros@gfz-postdam.de (P.A. Bedrosian).

0040-1951/$ - see front matter © 2004 Elsevier B.V. All rights reserved.
doi:10.1016/j.tecto.2004.02.010

1968). The mechanisms controlling which segments creep and which are locked are not well understood. It is likely that the composition of the wall rocks has some influence on seismic behavior. However, it has also been proposed that seismic behavior may be controlled by a fluid network within the fault zone. The ability of overpressured fluids to facilitate brittle failure at reduced effective normal stresses was first suggested by Rubey and Hubert (1959). Irwin and Barnes (1975) suggested the San Andreas fault creeps in regions where the Great Valley sequence (GVS) is cut by the fault. According to this hypothesis, the Franciscan complex is viewed as a source of aqueous fluids (derived from metamorphic reactions) which migrate into the San Andreas fault along the boundary between the Franciscan complex and the Great Valley sequence.

Recent studies, however, suggest that the role of fluids in faulting is more complicated than previously thought. High fluid pressure is an important component of the current debate concerning the strength of the SAF (Zoback et al., 1987; Mount and Suppe, 1987; Scholz, 2000; Townend and Zoback, 2000). In order to explain the apparent weakness of the SAF, complex models with spatially and/or temporally varying fluid pressure distributions are also called upon. Models by Sleep and Blanpied (1992) and Byerlee (1993) are based upon periodic fluid flow in the fault zone throughout the earthquake cycle. In such models, fluids are believed to enter the highly permeable and porous fault zone following an earthquake. Over time, shearing, creep compaction, and mineralization form low-permeability seals which isolate the fault zone from the surrounding country rock. Pore pressures then increase until rupture (an earthquake) occurs and the cycle begins again.

These models may explain both the apparent weakness of the SAF and its along-strike seismic variability. They suggest that significant permeability contrasts exist across the fault and that isolated, overpressured pockets of fluid might occur within the fault zone. The existence of these features is best examined through a combination of drilling and surface-based geophysical exploration.

Magnetotellurics (MT) is a geophysical technique for imaging subsurface resistivity structure using natural electromagnetic waves. Because the resistivity of crustal rocks is strongly influenced by fluid content, MT is well suited to imaging the presence and distribution of fluids within major fault zones. In the last decade, a number of MT studies have helped define the geometry and nature of the San Andreas fault zone in central California. Mackie et al. (1997) and Unsworth et al. (1999) imaged a narrow, low porosity San Andreas fault at Carrizo Plain, within the southern locked zone which last ruptured in the 1857 Fort Tejon earthquake. In contrast, magnetotelluric studies at Parkfield, within the transition zone between the creeping segment to the north and the locked segment to the south, imaged a prominent fault-zone conductor (FZC) extending to 3–4 km depth and attributed to 9–30% saline fluids (Unsworth et al., 1997, 2000). The first detailed MT study of the creeping central segment was described by Bedrosian et al. (2002) and imaged an extensive zone of enhanced electricalconductivity between the San Andreas and Calaveras faults, that extended to midcrustal depths beneath the SAF. Seismic tomography studies in the same location imaged a coincident zone of low V_p and high V_p/V_s, suggesting a fluid-rich region beneath and to the northeast of the SAF (Thurber et al., 1997). In this paper, a more detailed analysis of the MT data is presented. In combination with the seismic data, the geometry and distribution of fault-zone fluids are examined, and their implications for fault mechanics discussed.

2. Magnetotelluric data collection and analysis

The MT data were acquired in 1999 along two profiles that crossed the San Andreas and Calaveras faults (Fig. 1). The northern (Paicines) line crossed both the SAF and Calaveras faults about 20 km southeast of Hollister within the southern end of the Hollister Trough. The southern (Bear Valley) line crosses the same faults at the northern edge of the Pinnacle Volcanic formation, some 20 km further to the southeast. Continuous MT profiling, with electric dipoles laid end to end, was used within several kilometers of the major faults, and allows the problem of static shifts to be partially overcome. Vertical magnetic field variations were also recorded every 500–1000 m in the vicinity of the faults. The MT data were synchronously recorded with two ElectroMagnetic Instruments MT-24 systems at two sites (one on each profile) to allow for the removal of incoherent noise. This remote referencing technique was first

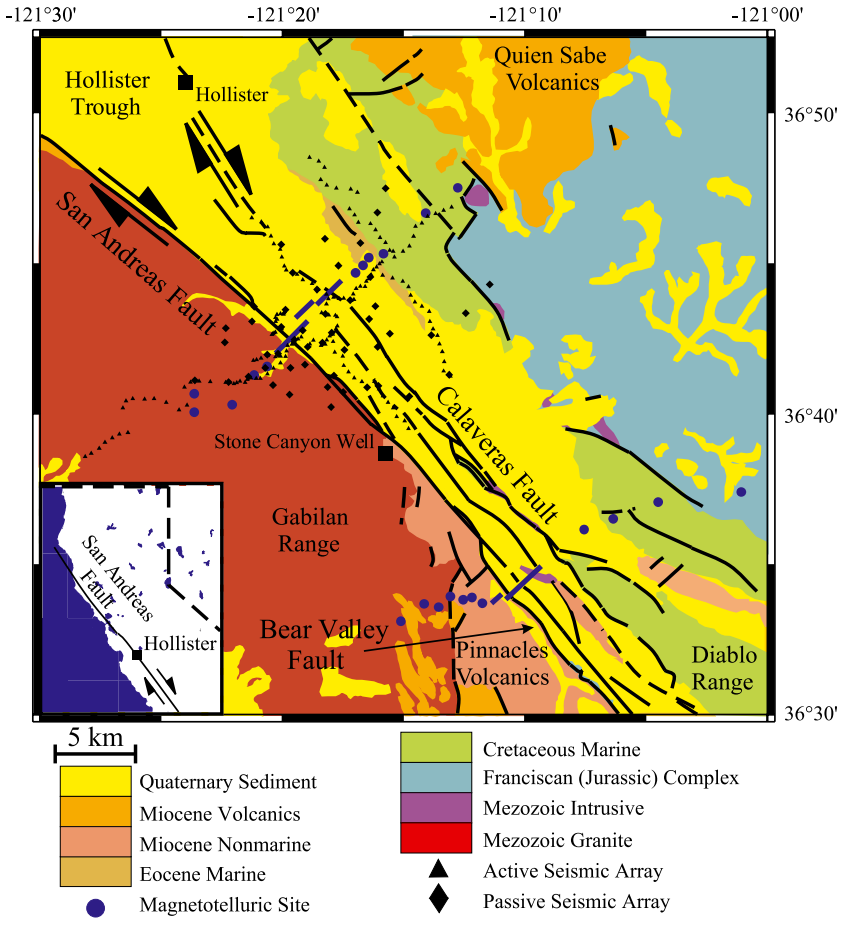

Fig. 1. Geologic map of the Hollister region based upon Wilson (1943). Outlined circles (blue in web version) indicate locations of magnetotelluric soundings. Thick lines (blue in web version) crossing the fault indicate regions of continuous MT data collection. Triangles and diamonds indicate locations of active and passive seismic arrays described in Thurber et al. (1997).

proposed by Gamble et al. (1979) based on data along the Bear Valley line. A continuously recording MT observatory at Parkfield (100 km from Hollister) was also employed to remove noise coherent over the length of the survey region (Boyd et al., 1997). In the following discussion, this site is referred to as the Parkfield reference site.

Electric and magnetic field time series were analyzed using the statistically robust algorithm of Egbert and Booker (1986) to compute MT transfer functions in the frequency range 100–0.001 Hz. Many sources of electromagnetic noise were present in the data due to the high population density of the survey region, just south of the San Francisco Bay Area. Much of the electromagnetic noise observed can be traced to power lines, transformers, well pumps, and electric fences, all of which produce noise well localized in either the time or frequency domain. Additionally, apparent resistivity data from a large percentage of sites on both profiles exhibit strong downward bias in the frequency range 1–0.1 Hz. This frequency range falls within the dead band, where signal to noise ratios are at a minimum. Because this noise was coherent over a length scale of just a few hundred meters, it was effectively removed through standard remote reference processing.

Electromagnetic noise coherent between two MT stations is more difficult to identify and separate from the MT signal. To assess the amount of coherent noise in the data, the multivariate processing code of Egbert

(1997) was employed. This makes use of multiple channels at multiple sites to determine the coherency of signal and noise within an array of synchronously recorded sites. With an array consisting of the Parkfield reference site and one or more sites from the Hollister survey area, we identified two coherent noise sources within the array. The first, prominent from 3 to 0.5 Hz, is coherent between sites in the Hollister area but incoherent with the Parkfield reference site, and hence separable from the MT signal. The second noise source, between 0.1 and 0.003 Hz, is coherent among all channels and sites within the array, and thus cannot be separated from the data. Egbert et al. (2000) attributed this noise to the Bay Area Rapid Transit system. For our purposes, the average power of this artificial EM signal is 10–20 dB less than the MT signal power and does not strongly bias MT transfer function estimates.

2.1. Dimensionality

The inversion of magnetotelluric data is greatly simplified if a two-dimensional (2D) analysis can be justified. Several methods were used to assess the dimensionality of the MT data from Hollister. The standard approach is to determine the geoelectric strike using tensor decomposition. In a 2D earth (where structure is uniform in one direction), geoelectric strike direction is well defined, frequency independent, and parallel to geologic strike. There is, however, a 90° ambiguity in the determined geoelectric strike. Another means of assessing dimensionality is skew, a frequency-dependent parameter derived from the MT transfer function (Swift, 1967). Skew, however, is rotationally invariant and thus cannot be used to determine the strike direction in a 2D case. Induction vectors (IV), computed from the ratio of vertical to horizontal magnetic fields (in the frequency domain) provide a final way of assessing dimensionality, and do not suffer from the 90° ambiguity. We look briefly at each of these in turn.

The geoelectric strike was calculated using two different tensor decompositions based upon the galvanic distortion model of Groom and Bailey (1989) (Smith, 1995; McNeice and Jones, 2001). Fig. 2

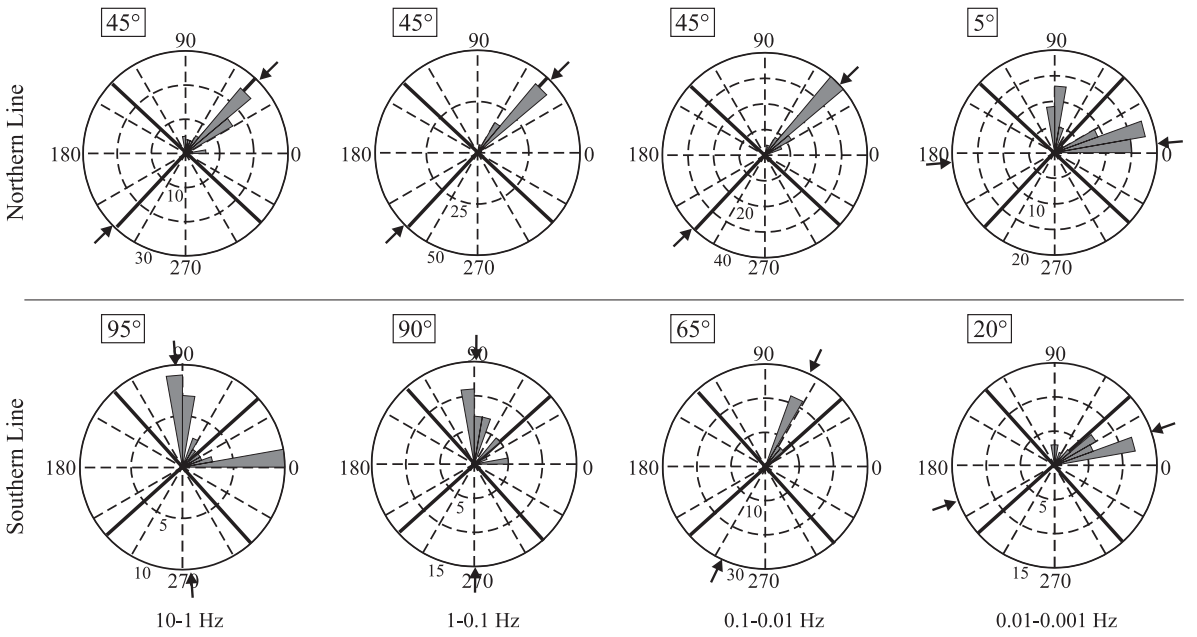

Fig. 2. Rose histograms of geoelectric strike for four frequency bands as calculated via tensor decomposition (Smith, 1995). Boxed numbers and arrows indicate the best fit geoelectric strike directions based upon 73 and 38 sites for the northern and southern profiles, respectively. Solid lines indicate geologic strike of the San Andreas fault (and orthogonal directions). A rotation of the geoelectric strike by 45° is observed between the lowest two frequency bands. Note the marked discrepancy at high frequencies between the two profiles.

shows histograms of the geoelectric strike direction in four frequency bands for one of these parameterizations. The higher frequencies sample near-surface structure, while lower frequencies are sensitive to deeper structure. Although not shown, results from the other decomposition agree to within 10° at all frequency bands on both lines.

Looking first to the northern profile, a well-defined strike direction of N45°E (or N45°W) is recovered within the frequency band 10–0.01 Hz. This corresponds to the seismically active fault zone (the surface to ~10-km depth). By comparison, the geologic strike of the SAF in this region is N47°W. There is, however, a 45° rotation in the geoelectric strike below a frequency of around 0.01 Hz. This transition frequency corresponds to skin depths of around 15 km to the NE of the fault, where the brittle–ductile transition occurs (Brace and Byerlee, 1970).

The calculated geoelectric strike for the southern profile is more complex. At lower frequencies, the geoelectric and geologic (N42°W near Bear Valley) strike directions are similar (within 20° of each other); however, at higher frequencies the geoelectric strike is oriented north–south (or east–west), perhaps reflecting near-surface structure. The southwestern half of this profile runs through east–west oriented Bickmore Canyon. An additional possibility is the proximity of this line to the Pinnacles Formation, Miocene volcanics cut by a series of north–south-trending faults. At the lowest frequency band examined, an ~45° rotation in geoelectric strike is observed, similar to that observed on the northern line.

As mentioned previously, skew can also be used to assess the dimensionality of MT data. Skew is only nonzero in the presence of three-dimensional (3D) earth structure, and thus large skew values are suggestive of deviation from our desired 2D earth. Fig. 3 plots skew as a function of frequency for sites along the northern profile. Similar results are observed for the southern profile (not shown). Note that the skew is generally small (≤ 0.2) above 0.01 Hz. The large skew values present below 0.01 Hz suggest 3D structure; however, it is important to note that MT measurements average over a large volume at these low frequencies, including all overlying structure. For example, 2D structure at depth (below ~0.01 Hz) oblique to the overlying 2D structure (defined by the SAF) would give rise to high skew values. Additionally, 3D structure to the side of an MT site are sensed by low frequency measurements; thus, high skew values at low frequencies may represent structural complexity at depth, beyond the ends of the profile, or both.

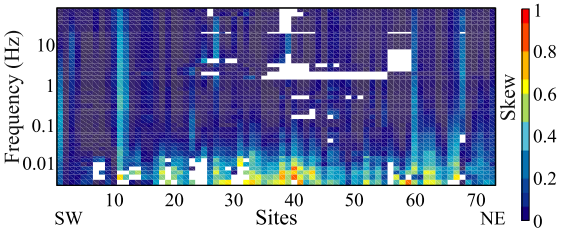

Fig. 3. Rotationally invariant, frequency-dependent skew at sites along the northern profile (Swift, 1967). White blocks indicate missing or bad data. Large values of skew indicate deviation of the measured impedance tensor from a 2D impedance tensor. Most data exhibit skew of less than 0.2, although a general increase is observed at low frequency.

Induction vectors (IV) provide a final means of assessing the dimensionality of the region. Over 2D structure, the real part of induction vectors are (a) oriented orthogonal to the geoelectric strike, (b) point toward conductive regions (Parkinson convention), and (c) are larger in resistive terrains (Parkinson, 1962; Wiese, 1962). Fig. 4 shows real induction vectors measured during the Hollister survey. At all but the lowest frequencies, the vectors are largest southwest of the fault, oriented roughly normal to the SAF, and generally point toward the fault. Consistent with geoelectric strike, the real induction vectors suggest a 2D earth (with a preferred strike parallel to the SAF) above ~15 km. Furthermore, the reversal of the IV implies a conductive feature is present within the locality of the SAF. Results from the southern profile again exhibit a more complex behavior, with a significant off-profile component to the IV at all frequencies. Finally, at the lowest frequency band examined ($f < 0.01$ Hz), the induction vectors southwest of the fault rotate by ~30° clockwise, while those northeast of the fault rotate counterclockwise by approximately the same amount. This change indirection at low frequencies is observed on both profiles, and indicates a departure from 2D earth structure.

From the above observations, we conclude that the regional geolectric structure is predominately 2D at frequencies above 0.01 Hz. Along the northern profile, geoelectric strike and induction vectors recover a

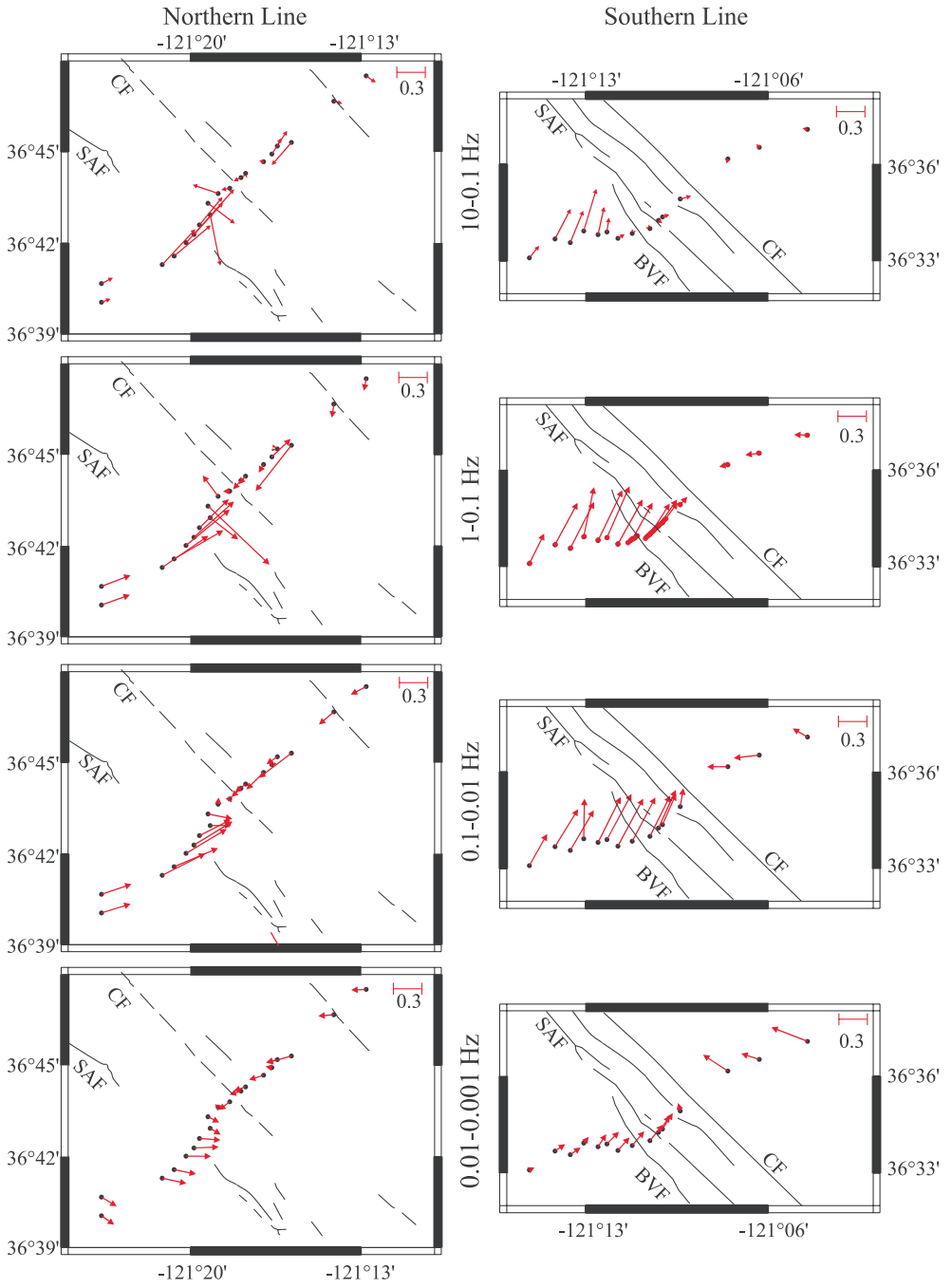

Fig. 4. Real induction vectors (Parkinson convention) within four frequency bands. At all but the lowest frequency band, induction vectors generally point toward the SAF and are largest on the resistive side of the fault.

strike direction of N40°W to N45°W, in agreement with the geologic strike of the SAF. Higher frequency data for the southern profile deviate from this picture, suggesting instead a north–south strike direction. Despite this discrepancy, we chose to apply 2D analysis and inversion to both profiles, rotating all data to a fault-oriented coordinate system. This is justified by the observation that above 1 Hz the southern line, data are nearly identical regardless of coordinate system. Furthermore, all inversions and models to be discussed are based only upon the sufficiently 2D data from 100 to 0.01 Hz. A discussion of the low frequency data is beyond the scope of this paper.

2.2. Magnetotelluric data

The data for both profiles are shown in pseudo-section format in Figs. 5 and 6, respectively. The apparent resistivity data for both TM and TE modes (currents flowing across- and along-strike, respectively) show a pattern of high resistivity southwest of the SAF, intermediate resistivity northeast of the Calaveras fault, and low resistivity between the two faults. The characteristic pattern seen in theTE mode phase, of high phases southwest of the fault and low phases northeast of the fault is observed on both profiles, and is indicative of a conductive fault zone. The bottom panels show the vertical magnetic field transfer function, T_z, which is sensitive to lateral resistivity contrasts. On the surface of a homogeneous or layered earth, this quantity is zero at all frequencies. Large values of T_z are observed predominantly in the case of 2D structure, where large along-strike currents can be produced. The large values observed ($\Re(T_z) \geq 0.5$) indicate strong lateral gradients in resistivity across the San Andreas and Calaveras faults.

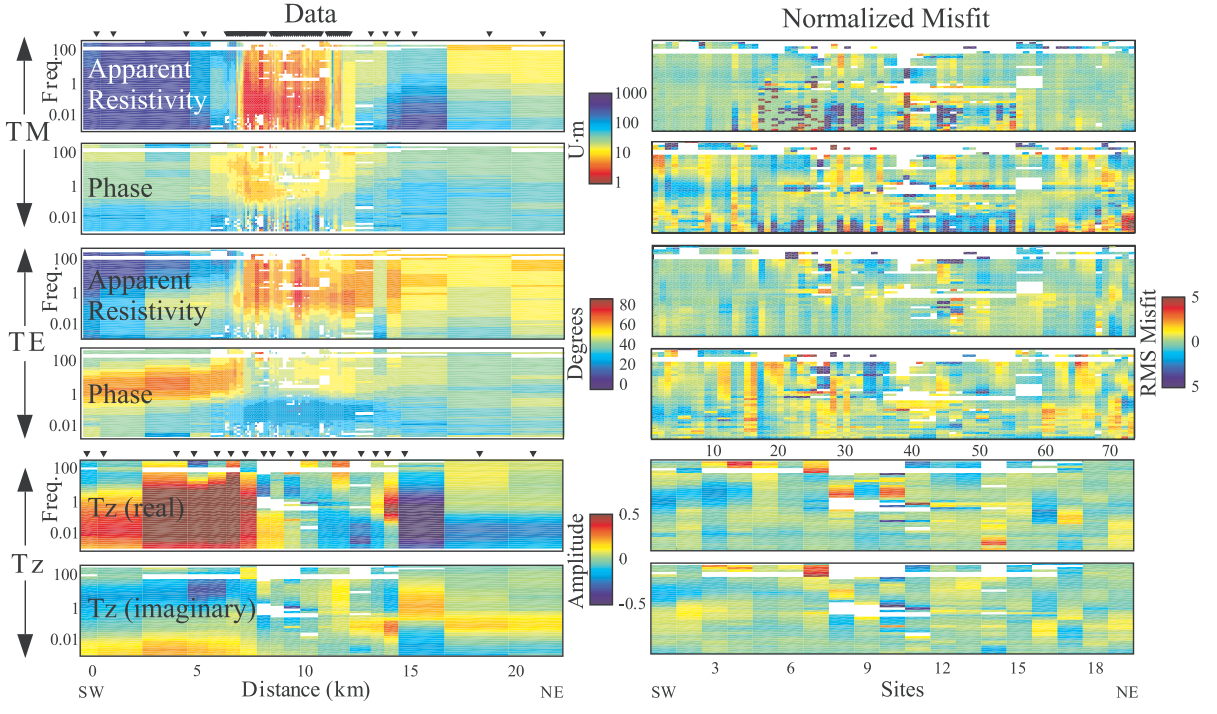

Fig. 5. MT data and normalized misfit of the best fitting model (Fig. 7a) for the northern profile. Because lower frequencies penetrate deeper into the earth, this display gives the impression of depth. Upper panels show apparent resistivity and phase for TM mode data where electric currents flow across the fault. Middle panels display apparent resistivity and phase for TE mode data where electric currents flow parallel to the fault. Lower panels show real and imaginary components of T_z (dimensionless). Inverted triangles indicate site locations and white regions indicate excluded data. Misfits are normalized by the larger of the data errors or the applied error floor. Misfits less then 1 fit the data to within the error bounds used in the inversion. Note that misfit sections are plotted versus site number rather than distance to better assess the fit.

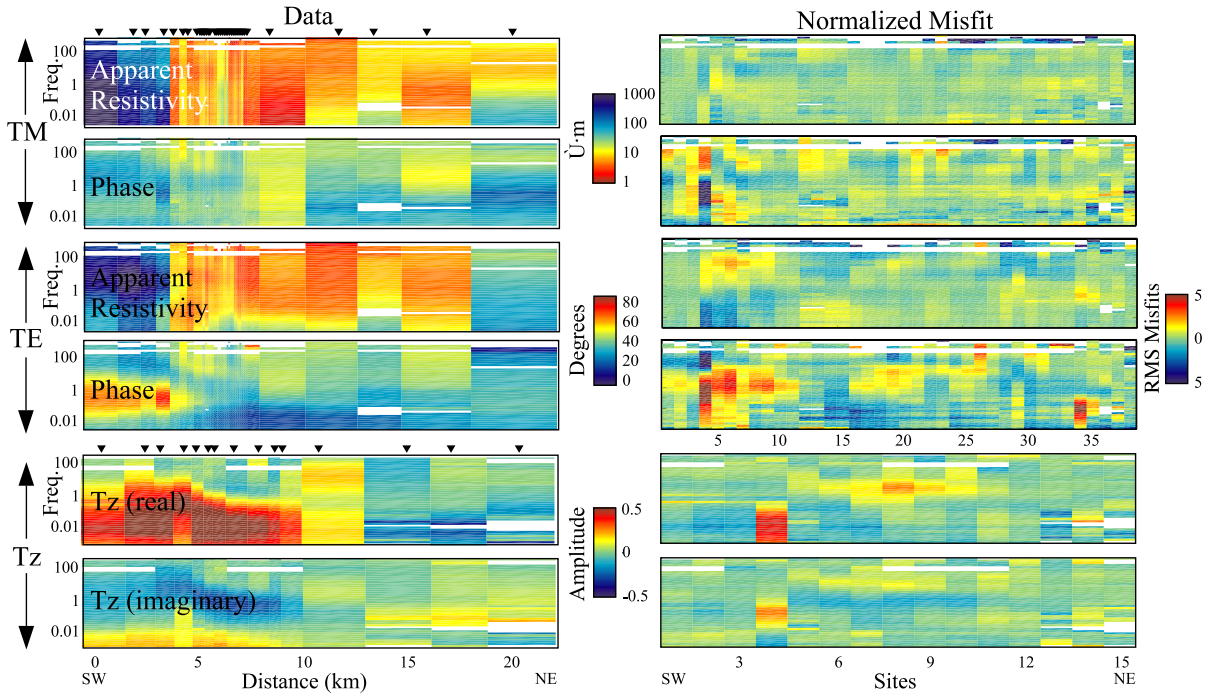

Fig. 6. MT data and normalized misfit of the best fitting model (Fig. 7b) for the southern profile. Presentation is analogous to that of Fig. 5 and details are described in the caption.

The MT and vertical magnetic field data were inverted using the regularized algorithm of Rodi and Mackie (2001). The trade-off between data misfit and model smoothness $[\nabla(\log\rho)^2]$ is controlled by the regularization parameter τ, determined through a series of trial inversions. The models shown in Fig. 7a and b result from inversions with τ equal to 50 and 10, respectively, and represent a compromise between data misfit and model smoothness. The models fit the TM mode, TE mode, and vertical magnetic field data to normalized r.m.s. misfits of 2.0 and 2.1 for the northern and southern lines, respectively. Error floors of 10% in apparent resistivity and 3° in phase were applied to the MT data, and an absolute error floor of 0.01 was placed on the T_z data. All data errors less than the prescribed error floor are replaced by the error floor; this ensures a uniform fit to the data at all frequencies. The small T_z error floor is needed to ensure these data are adequately fit, as there is no direct way to enforce the relative fitting of the MT and vertical field data. In reality, the T_z data errors are closer to 0.05, and this value is incorporated into subsequent misfit normalization.

The models shown in Fig. 7 result from a two step inversion process. Initial TM mode inversions starting from a 100 Ω m homogeneous half space model were used to identify first order model features. These broad features were then incorporated into starting models for the final inversions (TM + TE + T_z), but were not fixed during the inversion. The starting model for the northern line was a 500/50 Ω m quarterspace model with the boundary aligned with the surface trace of the SAF. The same model was used for the southern line, with the addition of a conductive (10 Ω m) basin in the upper 2 km NE of the SAF. The only feature fixed within the starting models is the Pacific Ocean, which is needed to accurately model the effects of the conductive ocean.

The normalized data misfits for both profiles are shown in Figs. 5 and 6. These residuals show that the data are well fit with respect to horizontal position and frequency. Misfits are normalized by the larger of the data errors or the applied error floor. As such, misfits

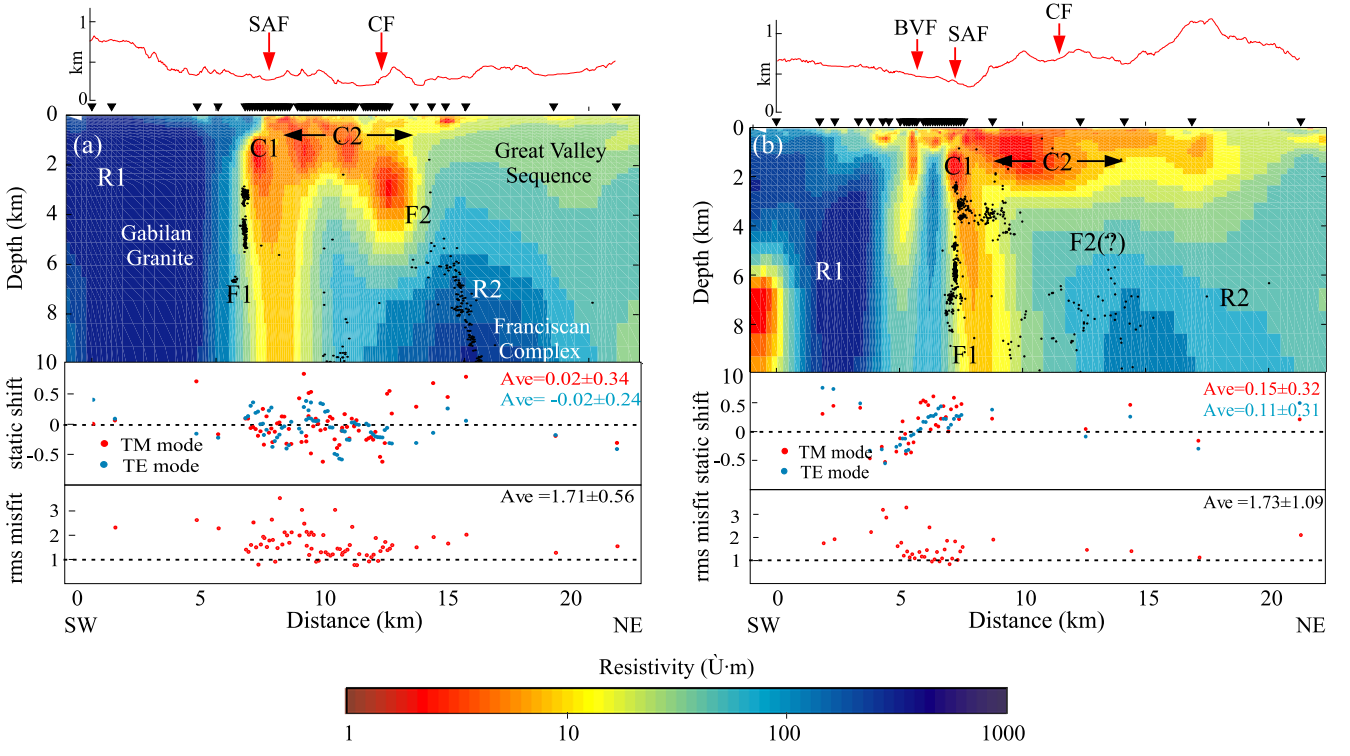

Fig. 7. Electrical resistivity models along the (a) northern and (b) southern profiles near Hollister, CA. Earthquake hypocenters within 1 km of each profile are shown as black circles. Inverted triangles indicate MT site locations. Red arrows mark surface traces of the San Andreas (SAF), Calaveras (CF), and Bear Valley (BVF) faults. Topography along profile is shown with a vertical exaggeration of 4:1. The models shown fit TM and TE mode data as well as vertical field data to normalized r.m.s. misfits of 2.0 and 2.1 on the northern and southern profiles, respectively. Site by site misfits and static shift parameters are shown for each model. Labeled features are discussed in the text.

less then 1 fit the data to within the error bounds used in the inversion. The average site misfit is 1.7 ± 0.6 on the northern line and 1.7 ± 1.1 on the southern line. Note that the overall misfit and the average site misfit are not directly comparable as they are calculated using different weightings.

Static shift parameters represent a frequency-independent gain in the previously described tensor decomposition. These parameters, one per mode at each site, cannot be directly determined from the decomposition, and were computed during the inversion. For the TM mode, in which electric currents flow along profile, continuous MT profiling (with a profile length much larger than the near-surface inductive length) imposes the constraint that the static shifts average to zero along profile. This constraint, the result of charge conservation, has been applied to both modes of the MT data, although in the case of the TE mode data it has no physical basis, and simply reduces the number of degrees of freedom by one.

3. Discussion

3.1. Regional geolectric structure

A resistive body (R1) is imaged southwest of the SAF on both profiles with resistivities greater than 1000 Ω m (Fig. 7). Constrained inversion studies show that R1 need not be as resistive as imaged; however, resistivities less than ~ 300 Ω m are in compatible with the data. R1 is coincident with the granodiorite of the Gabilan Range, part of the larger Salinian block cut by the SAF through much of central California (Ross, 1972). The uppermost few hundred meters are less resistive and corresponds to a surface-weathering zone. This uppermost layer is thicker on the southern profile, perhaps due to alluvium within Bickmore Canyon. R1 is uniform both along strike and with increasing depth, particularly along the northern profile. Coincident seismic studies by Thurber et al. (1997) also imaged a homogeneous velocity structure in this region.

Due to the high resistivity of R1, the natural EM signals penetrate to greater depths in this region than elsewhere on the profile, to depths of 50 km at the lowest frequencies used (~ 0.01 Hz). At a depth of approximately 6 km, the resistivity of R1 decreases at the southwest end of both profiles. While there is adequate penetration, the conductor beneath the Gabilan Range falls at the southwest edge of the profiles, and is constrained by only one site on each profile. Forward modeling studies indicate that this feature is not strongly required by the data, which can be equally fit by a conductor beyond the southwest end of our profiles. It is thus possible that we are imaging the relatively low resistivity of the coastal Franciscan block (Jennings, 1977).

A decrease in resistivity was also noted by Phillips and Kuckes (1983), who detected a conductive layer at ~ 13-km depth beneath the Gabilan range close to the northern profile. They hypothesized that the Gabilans are locally underlain by serpentinized ocean crust, a theory supported by seismic studies elsewhere within the Salinian block (Howie et al., 1993; Holbrook et al., 1996). Walter and Mooney (1982), however, argued instead that a granitic to gneissic transition is responsible for an increase in seismic velocity beneath the Gabilan range. It is interesting that this feature does not extend as far northeast as the SAF, but rather is separated from it by 6–8 km along both profiles.

Northeast of the Calaveras fault, crustal resistivities are moderate and increase with depth. The Franciscan complex is presumed to form the basement in this region, being locally overlain by the Cretaceous/Tertiary Great Valley sequence (GVS). Additionally, Quaternary sediments of the Hollister trough are adjacent to and cut by the SAF. The GVS is exposed in outcrop along the length of the Diablo Range and has a thickness of 6–8 km (Dickinson, 2002; Fielding et al., 1984). A strong resistivity gradient at 7–8-km depth to the northeast of the Calaveras fault may represent the boundary between the GVS and the underlying Franciscan complex.

An asymmetric region of enhanced electrical conductivity (C2) is found between the SAF and Calaveras fault. The geometry of this zone is similar on both profiles; its deepest part (C1) is located beneath the SAF and stops abruptly to the southwest. Such a sharp lateral resistivity variation is not imaged to the northeast. Coincident, asymmetric low-velocity zones have been imaged by Thurber et al. (1997) and Feng and McEvilly (1983) along the northern and southern profiles, respectively. The high-conductivity zone, C2, additionally appears to be divided into discrete pock-

ets divided by northeast dipping zones of higher resistivity. The resistivity of these zones drops to 1 Ω m, while the average is closer to 5 Ω m. A detailed discussion of the nature of this region is presented in the following sections.

To first order, the electrical structure observed is quite similar along the northern and southern profiles. Significant differences are, however, apparent between the two profiles. Crossing the southern profile, the Bear Valley fault (BVF) is located southwest of the San Andreas fault and runs parallel to it for ~ 15 km along strike. This fault shows no evidence of Holocene movement and even its very nature has been called into question by Dibblee (1966) who interprets it as an unconformity of nontectonic origin. Electrically, the BVF is imaged as a thin (~ 500 m wide) zone of enhanced conductivity extending to 2–3-km depth (Fig. 7), a signature suggestive of a tectonic origin for the BVF. The surface trace of the Bear Valley fault lies near the northeast edge of this zone.

A constrained inversion study was undertaken to determine if this conductor is a required feature of the model, or whether the data can be equally fit with a shallower conductor. The conductor imaged in Fig. 7b was truncated at a range of depths (0, 0.5, 1, 2.5 km depth) and the inversion restarted with the constraint that the resistivity model remain fixed in the region of modification. Visual inspection of a subset of the resulting models (Fig. 8) reveals that the misfit of the constrained inversion models differ minimally

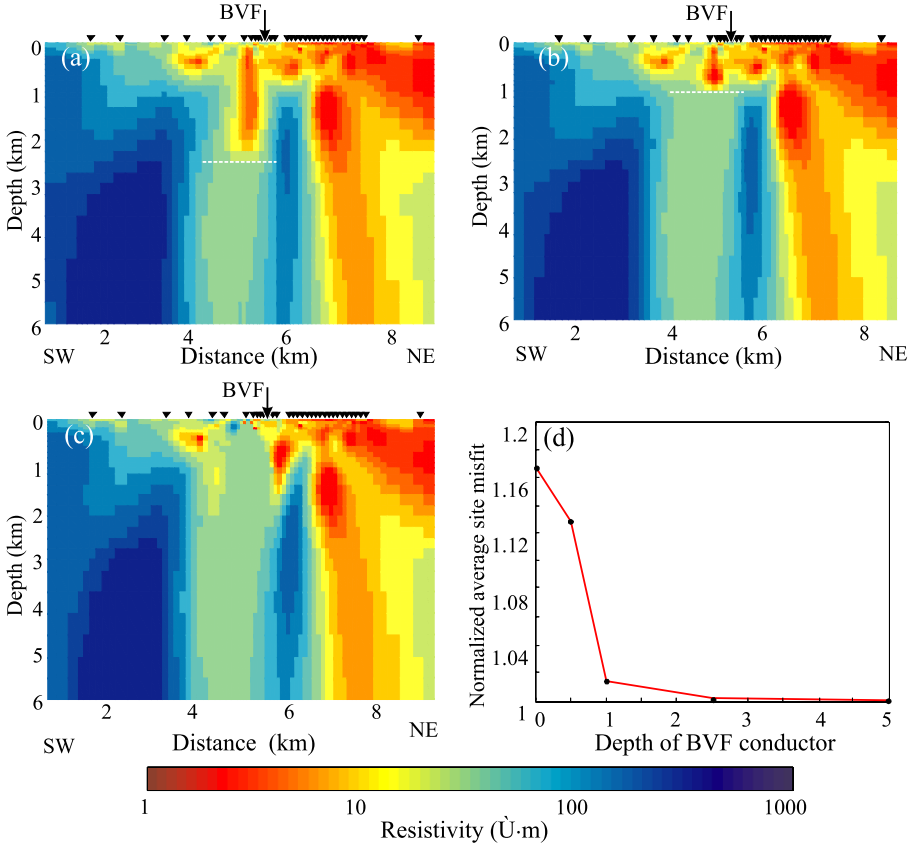

Fig. 8. Modified southern line resistivity models and associated misfit. Conductive zone adjacent to the Bear Valley fault has been truncated at a range of depths. Subsequent inversion of these models, with structure fixed below the truncation, gave rise to the above models. (a) Conductor terminated at 2.5 km, (b) conductor terminated at 1 km, (c) conductor completely removed, (d) average site misfit vs. depth of conductor. The average is taken over sites within 1 km of the conductor and is normalized to that of the best fit model (Fig. 7b). Arrow denotes location of BVF surface trace.

from the best fit model unless the conductor is terminated at 0.5-km depth or completely removed. In these two cases, increased conductivity is mapped onto neighboring structure, giving rise to conductive wings extending to 2-km depth. Fig. 8d shows the average site misfit (normalized to that of the best fit model) for sites located within 1 km of the conductor. Note the significant rise in site misfit when the conductor is truncated at depths shallower than 1 km. These studies suggest that the conductive halo extending to 5 km beneath the BVF is not a required feature of the model. However, the conductor adjacent to the BVF is a robust feature, and is required to extend to at least 1 km.

Below the imaged conductor, moderate resistivities appear to separate the Gabilan granites (R1) from a resistive sliver to the northeast. Further modeling found that the replacement of this gap with a resistive bridge is inconsistent with the data. This suggests that a fault slice may be bound between the Bear Valley and San Andreas faults; however, without knowing the depth extent of the BVF, such an assertion is speculative. To the east, the high-conductivity region, C2, extends at least 5 km east of the Calaveras fault, in contrast to the northern profile, where it terminates more abruptly at the Calaveras fault. Furthermore, on the southern profile, C2 appears relatively homogeneous. This, however, most probably reflects the sparsity of sites along this part of the profile rather than a lack of structural detail.

3.2. Fault-zone geometry

The resistivity models for both profiles suggest that zones of enhanced conductivity are bounded by the San Andreas and Calaveras faults; however, MT is not always able to delineate the edges of structures. In order to further evaluate the models, other geological and geophysical data were analyzed. This included (1) the regional seismicity, (2) seismic tomography, and (3) constrained MT inversion studies.

Seismicity along the SAF system is generally shallow; few regions exhibit seismicity below 10–15 km, the depth of the brittle–ductile transition (Brace and Byerlee, 1970). The resistivity models in Fig. 7 are overlain with the locations of earthquake hypocenters within 1 km of each profile ($M \geq 1.0$). Earthquake hypocenters have been relocated using the method of Waldhauser and Ellsworth (2000) applied to P-wave picks from the NCSN catalog (Ellsworth et al., 2000). Given the quality of the earthquake catalog, this method can determine relative hypocenter locations to within 25–50 m; however, the absolute location errors may be significantly larger (Bill Ellsworth, pers. comm.; Waldhauser and Ellsworth, 2002).

Seismicity on the SAF defines a near-vertical plane on both profiles, extending from 3 to 7 km depth on the northern line and 2–9 km depth on the southern line. On the northern line, seismicity lies $\sim$ 1.5 km southwest of the surface trace, a result also observed by Thurber et al. (1997) in determining hypocenters from a 2D velocity model. Further to the northeast, a northeast dipping (70°) plane of seismicity is evident on the northern line. As this seismicity is deeper (6–11 km) and not well localized, it is unclear to what mapped fault it projects. To the northwest, the seismicity appears associated with the Calaveras fault; however, it is located several kilometers northeast of the Calaveras surface trace. A linear projection of this seismicity to the surface falls within $\sim$ 500 m of the surface trace; however, this infers a significant dip to this predominantly strike-slip fault. Furthermore, earthquake focal mechanisms in the immediate region are in agreement with dextral strike-slip on vertical fault planes (Ellsworth, 1975). The solution may lie in the high spatial variability of seismicity along the southern Calaveras fault, with some areas devoid of seismicity, while others show events clustered along a vertical plane, and still others areas exhibit a prominently dipping fault plane. In the case at hand, the dipping fault can be traced for only 3–4 km alongstrike, and is thus most probably a local feature rather than a characteristic of the Calaveras fault.

The seismicity associated with the San Andreas fault locates at the southwest edge of conductive zone C1, hereafter referred to as the fault-zone conductor (FZC). This geometric relationship is seen on both profiles at Hollister (Bedrosian et al., 2002) as well as on a series of profiles at Parkfield (Unsworth et al., 1997), At Hollister, however, the FZC extends to greater depth than at Parkfield. It is also of note that little or no seismicity is seen within zones C1 and C2 on either profile. Finally, there is not a clear electrical signature of the Calaveras fault below 4 km. If the Calaveras fault is steeply dipping, as the seismicity

suggests, then there is no resistivity change associated with the fault as it cuts through the Franciscan (R2). If on the other hand, the Calaveras fault is vertical (and hence locally a seismic), then the moderate northeastward increase in resistivity at depth may represent different structural units juxtaposed across the fault.

While seismicity clearly marks the southwest boundary of the conductive zone, the bottom and northeast edge are not so well constrained. The coincident seismic tomography section of Thurber et al. (1997) is shown in Fig. 9 overlain upon the northern line resistivity model. Excellent correlation is observed between the two geophysical data sets. High resistivities (>1000 Ω m) and high P-wave velocities (>6 km/s) are imaged southwest of the fault, as expected for the Gabilan granites. A distributed zone of low V_p, high V_p/V_s, and low resistivity is present in the Hollister trough between the San Andreas and Calaveras faults, extending to 4–6 km depth. The most striking feature within this zone is the coincident low V_p and low resistivities that underlay the SAF to a depth of 8–10 km.

A histogram of the correlation between V_p and electrical resistivity in the upper 6 km of the northern line model is shown in Fig. 10. Two trends are observed; first, a general increase in electrical resistivity with increasing seismic velocity is apparent. A similar trend (blue curve in Fig. 10) has been observed by Dell'Aversana (2001) in well logs. The correlation occurs because a decrease in porosity produces an

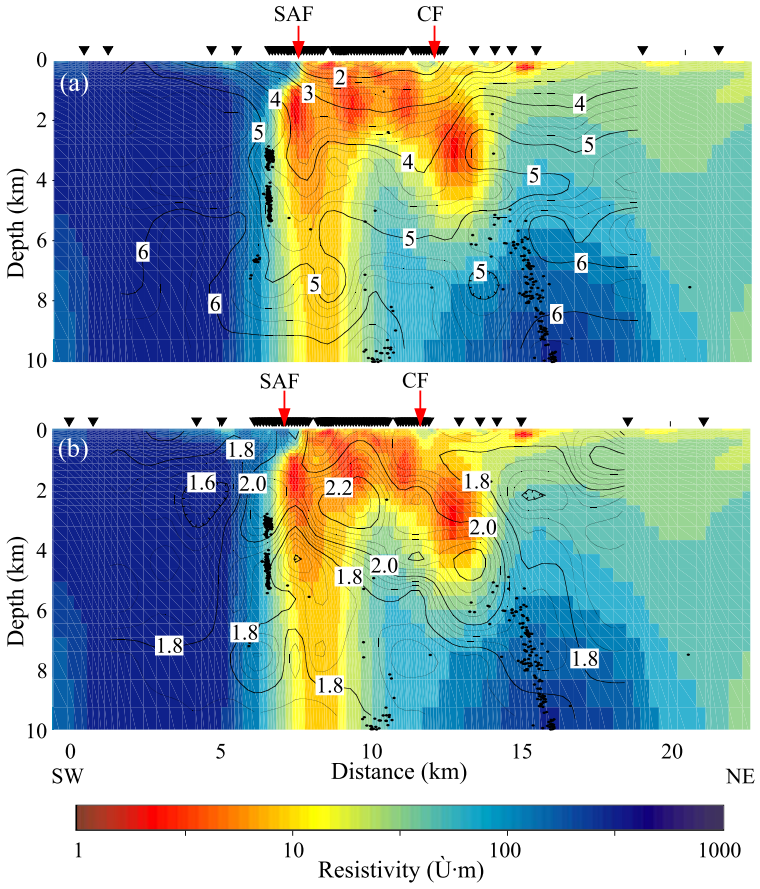

Fig. 9. Northern line model overlain with seismic tomography results from Thurber et al., 1997. (a) V_p contours, (b) V_p/V_s contours. Note the strong correspondence between the two data sets. Earthquake hypocenters within 1 km of each profile are shown as black circles. Inverted triangles indicate MT site locations. Red arrows indicate the surface traces of the San Andreas and Calaveras faults.

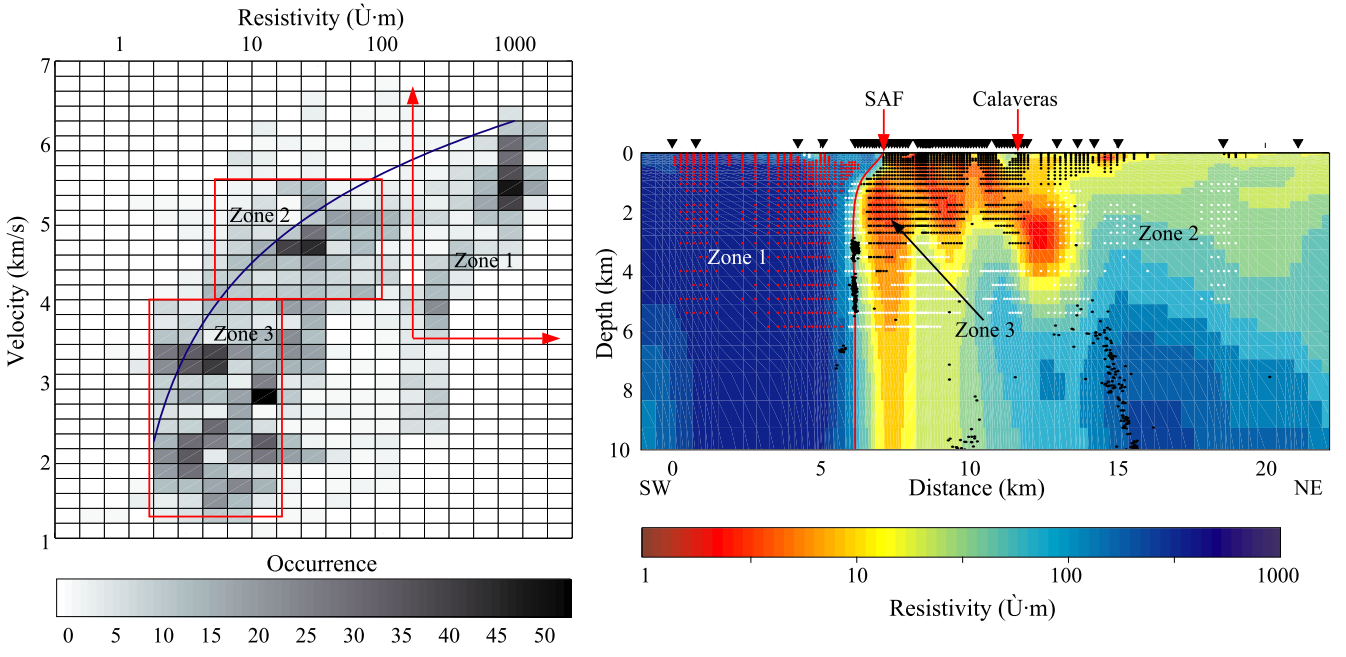

Fig. 10. Quantitative resistivity/velocity correlation. Histogram on left shows a general trend of increasing resistivity with increasing velocity, as well as three labeled zones of high correlation. Blue line indicates empirical resistivity/velocity correlation from Dell'Aversana (2001) based upon well log data. Right panel illustrates the spatial partitioning of the zones outlined at left. Zone 1 maps to the Gabilan granites; Zone 2 coincides with the Great Valley sequence excluding conductive regions C1 and C2; Zone 3 has pronounced low resistivities/velocities and is roughly coincident with regions C1 and C2. Large gaps in coverage are the result of different cell spacing in the seismic and MT models.

increase in both seismic velocity and resistivity. Second, localized zones of high correlation are observed. These are clusters showing common resistivities and velocities, and are not to be confused with previously described features (C1, C2, R1, R2) based solely on the MT models. Due to the coarse grid of the histogram (limited by the size of the seismic model grid), only three zones have been chosen. The right panel of Fig. 10 shows the spatial regions from which these zones derive. The region of high resistivity/velocity (zone 1) corresponds exclusively to the Gabilan granites. Zones 2 and 3 are defined by significantly lower resistivity/velocity and are located to the northeast of the SAF, overlaying large portions of the region between the SAF and Calaveras faults, as well as the upper 4 km northeast of the Calaveras.

The localization of these zones both spatially and in resistivity/velocity space suggest they delineate characteristic subsets of the data with (relatively) uniform material properties. For tectonic investigations, it is the boundaries between these zones that are of most interest. Zones 1 and 2 represent different geologic units (the Gabilan granites and the Great Valley sequence, respectively), while the boundary between zones 2 and 3 likely represents a hydrologic boundary between saturated and dry regions of the GVS. Hints of this undulating boundary are evident in the individual data sets; however, it is more clearly defined in this combined view. Additionally, the SAF is imaged as a narrow strip of low resistivity/velocity between zones 1 and 2, which also coincides with the plane of seismicity. Therefore, the combination of electrical and seismic data, along with seismicity patterns, are able to constrain the location of the San Andreas fault at depth to a narrow plane at the southwest edge of the imaged FZC.

Finally, the southwest boundary of zone 3 smoothly connects the surface trace of the SAF to the seismically defined SAF at depth. This southwest-dipping boundary is interpreted as the fault plane of the SAF in the upper 2 km. Gravity studies by Pavoni (1973) in the vicinity of the northern profile favor a steeply dipping (67–70°) SAF in the upper 5 km, with a vertical fault below. The MT data are inconsistent with a vertical SAF, and suggest a dip of 55° in the upper 2 km; however, a slightly steeper dip may be permissible. Assuming the density of zone 3 is less than zone 1 (a reasonable assumption given the much lower seismic velocity of zone 3), both the MT and gravity models emplace lower density material ~2 km southwest of the surface trace of the SAF. Given the appropriate density contrast across the fault, the geometry we image may be able to reproduce the measured gravity anomaly. In contrast, the MT model for the southern profile suggests a near vertical fault plane to within 1 km of the surface, above which no clear resistivity contrast is imaged. Seismic (Feng and McEvilly, 1983) and gravity (Wang et al., 1986) models of the Bear Valley profile also show a vertical SAF. Thus, the upper-crustal geometry of the San Andreas fault appears to vary significantly on a length scale of tens of kilometers.

While the above studies clearly delineate the lateral boundaries of C1 and C2, they are unable to constrain the depth extent of the fault-zone conductor (C1). To address this issue, a series of constrained inversions were performed in which the FZC was terminated at depths from 7 to 15 km. All of the constrained inversions produced models which fit the data equally well. Thus, based solely on data misfit, there is no reason to favor a particular model. Visual inspection of the resulting models (Fig. 11a–c) suggests that as the depth of the FZC decreases, its lateral extent and conductivity increase. This is an example of the sensitivity of magnetotellurics to the conductance, or integrated conductivity within a region. Fig. 11d shows the (horizontally integrated) conductance of the FZC for the three accompanying models as well as the (unconstrained) model from Fig. 7a. Observe that the deep conductance in the unconstrained model is pushed to shallower depths as the constraint is imposed. In the following section, we examine the origin of the enhanced conductivity and suggest that a deeper (yet narrower and less conductive) FZC may be more physically reasonable.

3.3. Origin of enhanced fault-zone conductivity

The analysis of the MT data described in this paper has shown that the fault-zone conductor is terminated abruptly to the southwest by the seismically defined SAF and extends to midcrustal depths. Additionally, the zones of high conductivity between the San Andreas and Calaveras faults extend no deeper than 4–6 km. What is the physical cause of the anomalously high conductivity of these zones?

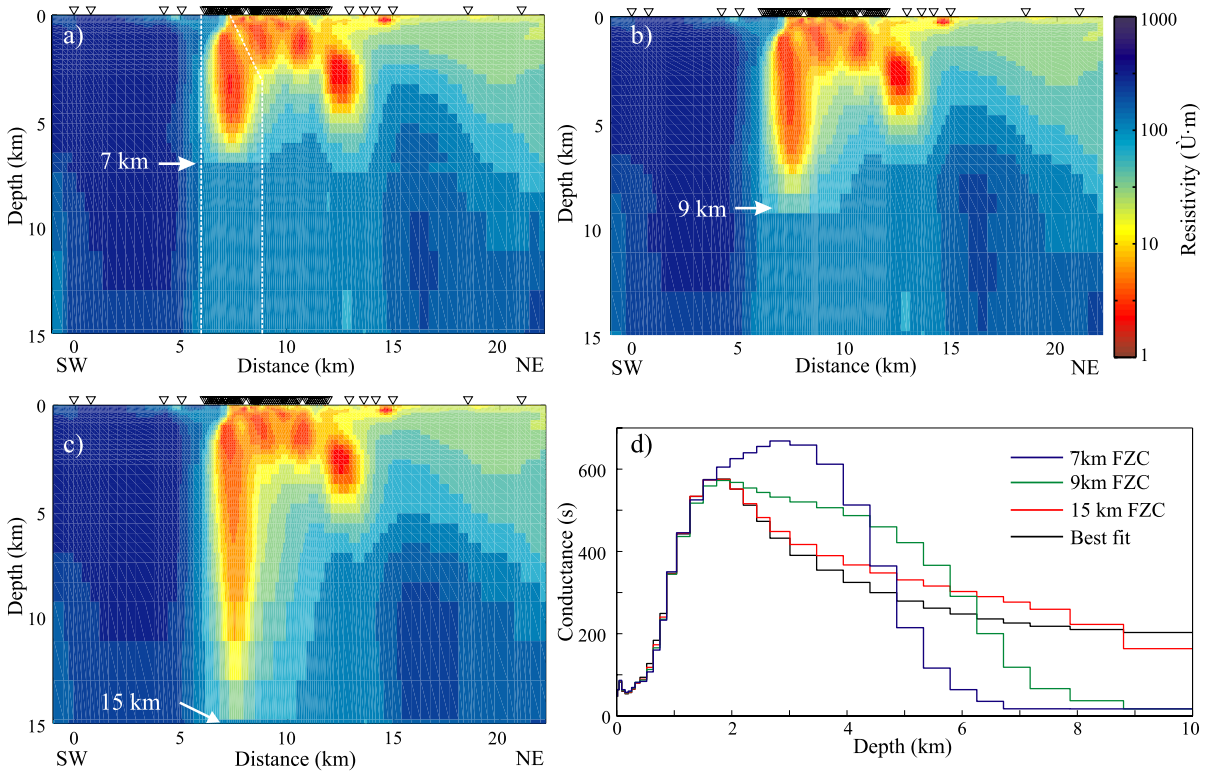

Fig. 11. Constrained inversion models and associated fault-zone conductances. (a–c) Inversion models with the fault-zone conductor (FZC) terminated at 7, 9, and 15 km depth. (d) Horizontally integrated conductance vs. depth for these models as well as the unconstrained model in Fig. 7a. White dotted lines delimit the region for which conductance has been calculated. Note that conductance is pushed to shallower depths as the constraint is imposed.

Our preferred explanation for the low resistivities imaged adjacent to the San Andreas fault is saline fluids. The fault-zone conductor imaged 100 km to the south at Parkfield was attributed to saline fluids within and surrounding the fault zone (Unsworth et al., 1999). The fluid is believed to be localized in breccia within the fault and the surrounding damage zone. To examine the potential role of fluids at Hollister, we first calculate the conductance of zones C1 and C2 to estimate the quantity of conductive material in the fault zone. Fig. 12 shows the conductance of the FZC as a function of depth for both profiles. The conductance peaks at 550 S on the northern profile and 900 S on the southern profile and can be compared with 1000–1500 S conductance distributed throughout C2 (not shown). In both zones and on both profiles, the conductance is greatest between depths of 1.5 and 2.0 km. Also shown in Fig. 12 is the depth distribution of earthquakes associated with the SAF. Note that a spatial separation exists between the depths of seismicity and peak fault-zone conductance. As conductance decreases with increasing depth, seismicity begins. This scenario is consistent with aqueous fluids as an explanation for the enhanced conductivity in C1 and C2. Fluid-rich regions are unlikely to maintain the shear stresses associated with brittle failure, and are thus devoid of seismicity. Adding to this picture are geochemical studies in the central Coast Ranges that find the source regions of saline springs to be generally aseismic yet surrounded by seismicity (Melchiorre et al., 1999).

Serpentinite, found frequently within the Franciscan complex and the overlying Coast Range ophiolite, has commonly been viewed as an alternative explanation for low resistivity. The low resistivity is not, however, due to the mineral itself, but rather arises

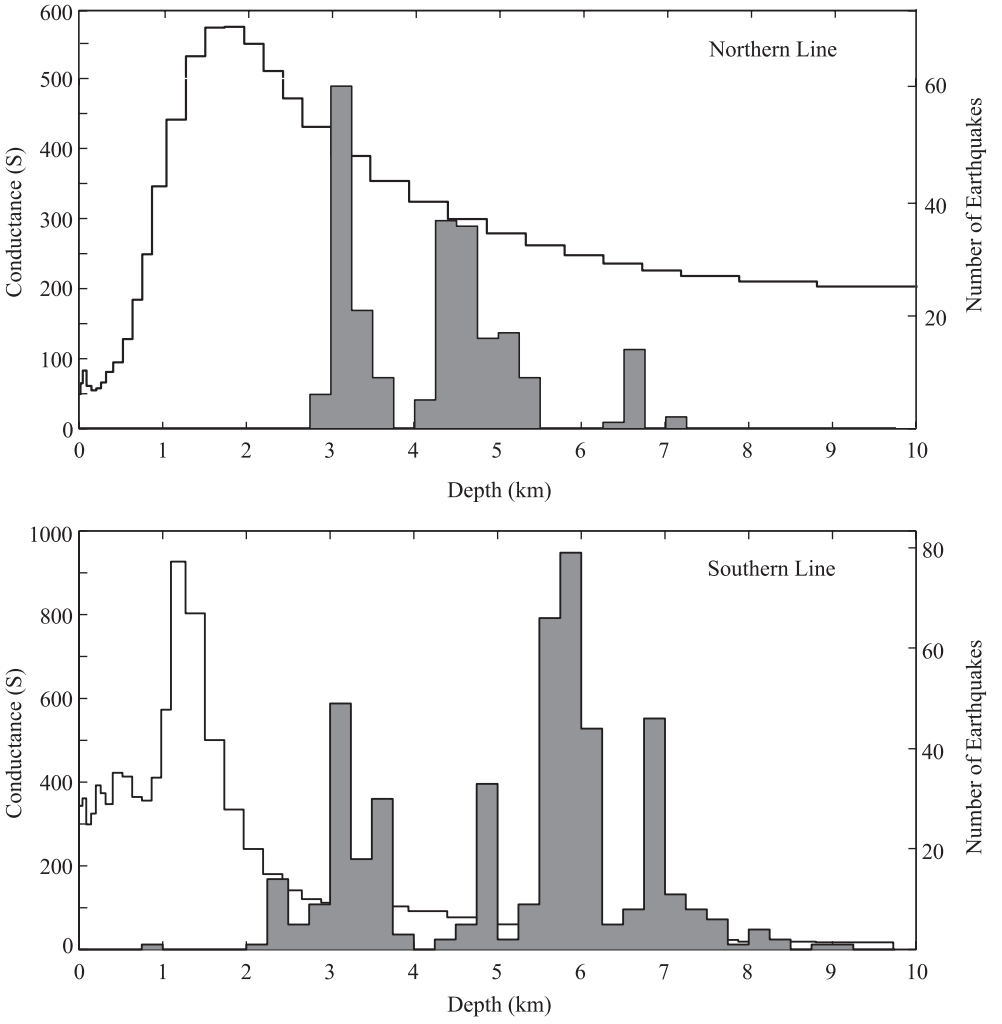

Fig. 12. Conductance (horizontally integrated conductivity) of the FZC as a function of depth. Conductance is observed to be largest between 0.5 and 2.5 km on both profiles. The histograms in gray show the distribution of earthquakes within 1 km of each profile (M>1.0) associated with the SAF. Note the spatial separation between the depths of high fault-zone conductance and high seismicity.

from the fluids released during its metamorphic conversion to olivine. Laboratory measurements of serpentinite-rich rocks containing a few percent magnetite, as are commonly found within the Coast Ranges, show resistivities of 10^4 Ω m or higher (Popp and Kern, 1993). Both the existence of serpentinite and the elevated temperatures (~ 500°) required to bring about its decomposition are needed in order to attain the low resistivities often attributed to it. As it is not intrinsically conductive, and temperatures in the upper crust are not high enough to activate its decomposition, we conclude that serpentinite is not a viable explanation for the imaged FZC at Hollister.

An entrained fault slice is another possible explanation for the anomalously low resistivities imaged. Throughout central California, fault slices are located between active and inactive strands of the San Andreas fault system. Slivers of igneous and metamorphic rocks (parts of the Salinian block, the Gold Hill gabbros) within the SAF system tend, however, to exhibit moderate to high resistivities. Pervasive fracturing (due to shearing) could significantly lower the

bulk resistivity; however, such fracturing would also weaken the sliver, making it unlikely to survive intact after significant transport along the fault. In short, given the degree of fracturing necessary to explain the low resistivity, any sliver would likely be ground up by the fault during transport.

Having discussed several alternative sources of high conductivity, were turn to aqueous fluids. How much fluid is needed to account for the observed resistivity? A porosity of 9–30%, saturated with aqueous fluids was necessary to explain the conductivity anomaly observed in the San Andreas fault at Parkfield (Unsworth et al., 1999). To relate electrical resistivity to porosity an estimate of the fluid salinity must be established. Salinities of 17 mg/l were measured in the Stone Canyon well, a 600-m-deep artesian well located within the Gabilan granite (Fig. 1) midway between the two profiles and 1 km from the SAF (Stierman and Williams, 1984; J. Thordsen, pers. comm.). Archie's law can be used torelate the fluid resistivity (a function of salinity and temperature) and porosity of a fluid saturated rock to its bulk resistivity. Combining the average resistivity (5 Ω m) of the FZC at 1.5-km depth (the depth of peak conductance) with the salinity from the Stone Canyon well, a porosity range of 15–35% is obtained. The limits reflect the geometry of the pores; upper and lower limits correspond to spherical pores and cracks, respectively, the latter being a reasonable assumption surrounding an active fault zone. It should be noted that these estimates place an upper bound on porosity, as the presence of clay minerals within the fault zone will further decrease electrical resistivity. It is unclear, however, how to quantitatively address either the amount and distribution of clay in the fault zone or its effect on resistivity. That the stated porosities represent an upper bound is additionally based upon fluid salinities. Salinities are generally higher on the northeast side of the fault, as at the Varian well near Parkfield (Jongmans and Malin, 1995), and increasing fluid salinity decreases the required porosity. Unfortunately, salinity measurements from the northeast side of the fault are not available within the survey region.

The porosities estimated at shallow depths are in agreement with independent porosity estimates. Gravity studies in Bear Valley by Wang et al. (1986) suggest a low-density wedge centered on the San Andreas fault zone extending to the base of the seismogenic zone. The authors calculate a lower porosity bound of 12% for this region; however, the modeling assumes a constant density (and hence porosity) from the surface to ~15-km depth. In reality, a decrease in porosity is expected with increasing depth as confining pressure increases. At depths approaching the brittle–ductile transition, the resistivity of the fault zone increases to around 10 Ω m. The effect of increasing pressure and temperature, however, cause fluid resistivity, and in turn bulk resistivity, to decrease. Taken together, the MT data suggest porosities of 2–15% at 10 km depth beneath the SAF. We again favor the lower end of this range for the reasons cited above. The presence of a few percent porosity at such depths may result from small and recoverable volumetric strain due to shearing.

At this point, we revisit the question of the depth extent of the fault-zone conductor. As discussed before, limiting the depth extent of the FZC results in a broadening and intensification of the remaining structure. This results in higher porosities being required to explain the low resistivity. For example, if the FZC is terminated at 7 km depth as in Fig. 11a, porosities of up to 50% at 1.5 km and 15% at 5 km depth are needed. As these values appear unrealistic, we favor a model with a narrower and deeper FZC (Fig. 11c) which requires more moderate porosities to account for the decreased resistivity within the fault zone.

The source of fault-zone fluids remains uncertain. Irwin and Barnes (1975) suggest they may emanate from metamorphic reactions within the Franciscan complex, transported laterally into the fault zone. Geochemical studies of fault-zone materials by Pili et al. (1998) support this conclusion and suggest that during deformation the fault zone is infiltrated by mixed H_2O-CO_2 fluids of metamorphic or deep crustal origin. In contrast, the geochemical signature of spring and well fluids along the SAF suggest a meteoric fluid origin, with a maximum circulation depth of 6 km (Kharaka et al., 1999). This is comparable to the depth at which estimated porosities fall below 10%. Finally, a high flux of mantle-derived CO_2 is inferred by Kennedy et al. (1997) based on helium isotopic ratios in springs and seeps along the SAF.

To interpret the electrical images of the San Andreas, it is essential to compare the geophysical

models with geological observations of exhumed fault zones (Chester and Logan, 1986; Chester et al., 1993). The highest conductivities are observed in the upper 2–3 km of the San Andreas fault, both at Parkfield and Hollister. As described above, relatively high porosities are required to account for the observed low resistivity. Thus, the shallow part of the fault zone is probably a zone of fault breccias (Anderson et al., 1983). This is surrounded by the damage zone, a region of pervasive fracturing (Caine et al., 1996). Saline fluids present in the fault will readily fill voids in the breccia and fractures within the damage zone, resulting in the observed low resistivity. As depth increases, geological studies have shown that cataclasites and mylonites are formed in the fault zone at higher ambient pressure and temperature. These are presumably present in the creeping San Andreas fault at Hollister in the 4–10-km depth range. The resistivity models derived from the MT data show that significant porosity is present in this depth range where the fault may be expressed as a distributed zone of shearing.

The abrupt southwest boundary of C1 and the sharp northeast dipping boundaries within C2 (cutting stratigraphic horizons) suggest that fluid distribution is tectonically controlled. Other studies have indicated that faults can act both as conduits for along-strike fluid flow and as barriers for across-strike flow (Ritter et al., 2003; Caine et al., 1996). We conclude that the dipping boundaries within C2 represent fault seals separating pockets of fluid-saturated rock. Our 2D profiles cannot address whether these faults additionally act as conduits, but 3D tomographic modeling images a continuous low V_p zone extending for at least 10 km along strike.

4. Conclusions

Based upon the MT and seismic studies at Hollister, an integrated geophysical model is proposed (Fig. 13) for the northern profile. Within the creeping segment south of Hollister, CA, the San Andreas fault is characterized by a zone of low resistivity extending from the San Andreas fault to the Calaveras fault. This zone of low resistivity is imaged on both profiles and in the upper 2–3 km is attributed to fluid filled voids and fractures within the brecciated and damaged zone of the fault (Caine et al., 1996; Anderson et al., 1983). These conductivity values can be accounted for by a porosity of 15–35% of aqueous fluids. These values represent an upper bound due to the possible effect of clays within the fault zone. The conductance of the fault zone decreases with depth, but the conductivity remains significantly higher than expected for dry

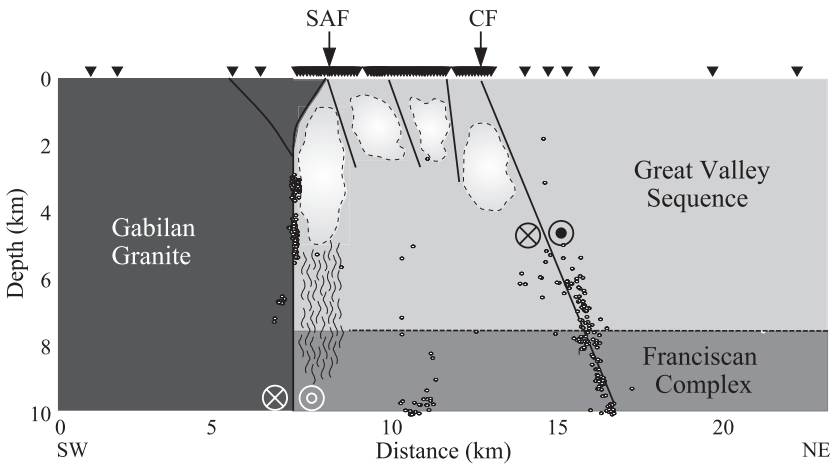

Fig. 13. Geophysical model of the San Andreas fault-zone along the northern profile. Surface traces of San Andreas (SAF) and Calaveras (CF) faults are denoted. White circles indicate seismicity within 1 km of the profile. Dashed zones denote fluid-saturated regions with porosities of 15–35%. The most extensive zone is located adjacent to the SAF and is attributed to fluid filled voids and fractures within the damage zone of the fault. High conductivity at greater depths is attributed to fluid-filled, fault-aligned cracks within a broad zone of shearing.

midcrustal rocks. This is possibly due to 2–15% fluids present in fault aligned cracks.

The combination of seismic and magnetotelluric data has determined that the SAF is vertical below 2 km depth, and is located on the southwest edge of the imaged fault-zone conductor. The low resistivity between the San Andreas and Calaveras faults is distributed in localized zones interpreted as fluid pockets separated from one another by northeast dipping, impermeable fault seals. In combination with previous MT studies at Carrizo Plain and Parkfield, these results suggest a relationship between seismicity and fluid supply from the Franciscan complex to the fault zone. At Parkfield and Hollister where the fault creeps, the breccia and damage zones are saturated with fluids (presumably derived from the Franciscan complex). In contrast, at Carrizo Plain the east wall of the San Andreas fault is resistive, crystalline rock devoid of fluid pathways. The fault here is locked and fractures in the damaged zone are relatively dry.

How is the fluid regime of the San Andreas fault related to it's seismic behavior? In one scenario, fluids could be controlling the seismic behavior. It should be noted that the FZC, and thus the inferred fluids, is best resolved at relatively shallow depths, well above the source region of major earthquakes. However, a fluid saturated shallow fault zone suggests fluids could be present at greater depth. These fluids, if isolated and over pressured, may control the mechanics of faulting as envisioned by Byerlee (1993) and Sleep and Blanpied (1992). In this scenario, significant changes in the electrical structure of the San Andreas fault may be observable immediately following a moderate to large earthquake in central California. Unfortunately, MT can only image the distribution of fluids within and surrounding the fault zone; in situ studies alone are able to determine whether such fluids are at or above hydrostatic pressure. In an alternate scenario, fluids surrounding the SAF may simply be a consequence of a creeping fault rather than a controlling factor. A segment of the fault that is creeping is likely to develop and maintain an interconnected network of fractures. When saline groundwater fills these cracks, the resistivity decreases. Further understanding of these phenomena will require additional geophysical data. This includes 3D studies of the San Andreas and other major strike-slip faults, and studies of the same location throughout the seismic cycle.

Acknowledgements

The MT component of this study was supported by DOE Grant DEEG03-97ER-14781, NSF grant EAR9614411, and USGS grants 1434-HQ-97-GR-03157and 1434-HQ-97-GR-03152. The seismic component was supported by NSF grant EAR-9317030 with additional support from the Deep Continental Studies program of the USGS. The seismic instruments used were provided by the PASSCAL facility of IRIS. MT instruments were provided by the EMSOC consortium. Parkfield MT data were provided courtesy of the Berkeley Seismological Laboratory. Earthquake hypocenters are from the Northern California Seismic Network. Both of these data sets are archived and distributed by the Northern California Earthquake Data Center. We wish to thank the area landowners who graciously allowed access to their property, and to T. Burdette for assistance with permitting. Finally, this study would not have been possible without much enthusiastic field help (Sierra Boyd, Jerry Casson, Shawn Cokus, Nick Hayman, Michelle Koppes, Shenghui Li, Gillian Sharer, and John Sylwester). We thank Stephen Park and Mark Zoback for their reviews and Associate Editor Tuncay Taymaz for suggestions, both of which greatly improved this paper.

References

Allen, C., 1968. The tectonic environments of seismically active and inactive areas along the San Andreas fault system. In: Dickinson, W.R., Grantz, A. (Eds.), Proceedings of Conference on Geologic Problems of the San Andreas Fault System. Stanford University Publications, pp. 70–82.

Anderson, J.L., Osbourne, R.H., Palmer, D.F., 1983. Cataclastic rocks of the San Gabriel fault: an expression of deformation at deeper levels in the San Andreas fault zone. Tectonophysics 98, 209–251.

Bedrosian, P.A., Unsworth, M.J., Egbert, G., 2002. Magnetotelluric imaging of the creeping segment of the San Andreas fault near Hollister. Geophys. Res. Lett. 29, 1–4.

Boyd, O.S., Egbert, G.D., Eisel, M., Morrison, H.F., 1997. A preliminary analysis of the Parkfield EM field monitoring network. EOS Trans. AGU 78, 489.

Brace, W.F., Byerlee, J.D., 1970. California earthquakes: why only shallow focus? Science 168, 1573–1575.

Byerlee, J., 1993. Model for episodic flow of high-pressure water in fault zones before earthquakes. Geology 21, 303–306.

Caine, J.S., Evans, J.P., Forster, C.B., 1996. Fault zone architecture and permeability structure. Geology 24, 1025–1028.

Chester, F.M., Logan, J.M., 1986. Implications for mechanical properties of brittle faults from observations of the Punchbowl fault zone, California. Pure Appl. Geophys. 124, 79–106.

Chester, F.M., Evans, J.P., Biegel, R.L., 1993. Internal structure and weakening mechanisms of the San Andreas fault. J. Geophys. Res. 98, 771–786.

Dell'Aversana, P., 2001. Integration of seismic, MT, and gravity data in a thrust belt interpretation. First Break 19, 335–341.

Dibblee Jr., T.W., 1966. Evidence for cumulative offset on the San Andreas fault in central and northern California. Bull.-Calif., Div. Mines Geol. 190, 375–384.

Dickinson, W.R., 2002. Reappraisal of hypothetical Franciscan thrust wedging at Coalinga: implications for tectonic relations along the Great Valley flank of the California Coast Ranges. Tectonics 29 (doi: 10.1029/2001TC001315).

Egbert, G.D., 1997. Robust multiple station magnetotelluric data processing. Geophys. J. Int. 130, 475–496.

Egbert, G.D., Booker, J.R., 1986. Robust estimation of geomagnetic transfer functions. Geophys. J. R. Astron. Soc. 87, 173–194.

Egbert, G.D., Eisel, M., Boyd, O.S., Morrison, H.F., 2000. DC trains and PC3s: source effects in mid-latitude geomagnetic transfer functions. Geophys. Res. Lett. 27, 25–28.

Ellsworth, W.L., 1975. Bear Valley, California, earthquake sequence of February–March 1972. Bull. Seismol. Soc. Am. 65, 483–506.

Ellsworth, W.L., Beroza, G.C., Julian, B.R., Klein, F., Michael, A.J., Oppenheimer, D.H., Prejean, S.G., Richards-Dinger, K., Ross, S.L., Schaff, D.P., Waldhauser, F., 2000. Seismicity of the San Andreas Fault system in central California: application of the double-difference location algorithm, on a regional scale. EOS, Trans. AGU 81 (48), 919.

Feng, R., McEvilly, T.V., 1983. Interpretation of seismic reflection profiling data for the structure of the San Andreas fault zone. Bull. Seismol. Soc. Am. 73, 1701–1720.

Fielding, E., Barazangi, M., Brown, L., Oliver, J., Kaufman, S., 1984. COCORP seismic profiles near Coalinga, California: subsurface structure of the western Great Valley. Geology 12, 268–273.

Gamble, T.D., Goubau, W.M., Clarke, J., 1979. Magnetotellurics with a remote reference. Geophysics 44, 53–68.

Groom, R.W., Bailey, R.C., 1989. Decomposition of magnetotelluric impedance tensors in the presence of local three-dimensional galvanic distortion. J. Geophys. Res. 94, 1913–1925.

Holbrook, W.S., Brocher, T.M., ten Brink, U.S., Hole, J.A., 1996. Crustal structure of a transform plate boundary: San Francisco bay and the California continental margin. J. Geophys. Res. 101, 22311–22334.

Howie, J.M., Miller, K.C., Savage, W.U., 1993. Integrated crustal structure across the south central California margin: Santa Lucia escarpment to the San Andreas fault. J. Geophys. Res. 98, 8173–8196.

Irwin, W.P., Barnes, I., 1975. Effect of geologic structure and metamorphic fluids on seismic behavior of the San Andreas fault system in Central and Northern California. Geology 3, 713–716.

Jennings, C.W., 1977. Geologic map of California, California Geological Survey, scale 1:750,000.

Jongmans, P.A., Malin, P.E., 1995. Microearthquake S-wave observations from 0 to 1 km in the Varian well at Parkfield, California. Bull. Seismol. Soc. Am. 85, 1805–1821.

Kennedy, B.M., Kharaka, Y.K., Evans, W.C., Ellwood, A., DePaolo, D.J., Thordsen, J., Ambats, G., Mariner, R.H., 1997. Mantle fluids in the San Andreas fault system, California. Science 278, 1278–1281.

Kharaka, Y.K., Thordsen, J.J., Evans, W.C., Kennedy, B.M., 1999. Geochemistry and hydromechanical interactions of fluids associated with the San Andreas fault system, California. In: Haneberg, W.C., Mosely, P.S., Moore, J.C., Goodwin, L.B. (Eds.), Faults and Subsurface Fluid Flow in the Shallow Crust. Geophysical Monograph, vol. 113. American Geophysical Union, Washington, pp. 129–148.

Mackie, R.L., Livelybrooks, D.W., Madden, T.R., Larsen, J.C., 1997. A magnetotelluric investigation of the San Andreas fault at Carrizo Plain, California. Geophys. Res. Lett. 24, 1847–1850.

McNeice, G.W., Jones, A.G., 2001. Multisite, multifrequency tensor decomposition of magnetotelluric data. Geophysics 66, 158–173.

Melchiorre, E.B., Criss, R.E., Davisson, M.L., 1999. Relationship between seismicity and subsurface fluids, central Coast Ranges, California. J. Geophys. Res. 104, 921–939.

Mount, V.S., Suppe, J., 1987. State of stress near the San Andreas fault: implications for wrench tectonics. Geology 15, 1143–1146.

Parkinson, W.D., 1962. The influence of continents and oceans on geomagnetic variations. Geophys. J. 2, 441–449.

Pavoni, N., 1973. A structural model for the San Andreas fault zone along the northeast side of the Gabilan Range. In: Kovach, R.L., Nur, A. (Eds.), Proceedings of Conference on Tectonic Problems of the San Andreas Fault System. Stanford Univ. Publication, Stanford, CA, pp. 259–267.

Phillips, W.J., Kuckes, A.F., 1983. Electrical conductivity structure of the San Andreas fault in central California. J. Geophys. Res. 88, 7467–7474.

Pili, E., Kennedy, B.M., Conrad, M.S., Gratier, J.P., 1998. Isotope constraints on the involvement of fluids in the San Andreas fault. EOS, Trans. AGU 79, 229–230.

Popp, T., Kern, H., 1993. Thermal dehydration reactions characterized by combined measurements of electrical conductivity and elastic wave velocities. Earth Planet. Sci. Lett. 120, 43–57.

Ritter, O., Weckmann, U., Hoffmann-Rothe, A., Abueladas, A., Garfunkel, Z., DESERT Research Group, 2003. Geophysical images of the Dead Sea Transform in Jordan reveal an impermeable barrier for fluid flow. Geophys. Res. Lett. 30 (doi: 10.1029/2003GL017541).

Rodi, W., Mackie, R.L., 2001. Nonlinear conjugate gradients algorithm for 2-D magnetotelluric inversion. Geophysics 66, 174–187.

Ross, D.C., 1972. Geologic Map of the Pre-Cenozoic Basement Rocks, Gabilan Range, Monterey and San Benito Counties, California. United States Geological Survey, Map MF-357.

Rubey, W.W., Hubbert, M.K., 1959. Role of fluid pressure in mechanics of overthrust faulting. Bull. Geol. Soc. Am. 70, 167–206.

Scholz, C.H., 2000. Evidence for a strong San Andreas fault. Geology 28, 163–166.

Sleep, N.H., Blanpied, M.L., 1992. Creep, compaction and the weak rheology of major faults. Nature 359, 687–692.

Smith, J.T., 1995. Understanding telluric distortion matrices. Geophys. J. Int. 122, 219–226.

Stierman, D.J., Williams, A.E., 1984. Hydrologic and geochemical properties of the San Andreas fault at the Stone Canyon well. Pure & Appl. Geophys. 122, 403–424.

Swift, C.M., 1967. A magnetotelluric investigation of an electrical conductivity anomaly in the southwestern United States. PhD thesis, Mass. Inst. Technology.

Thurber, C., Roecker, S., Ellsworth, W., Chen, Y., Lutter, W., Sessions, R., 1997. Two-dimensional seismic image of the San Andreas fault in the Northern Gabilan Range, central California: evidence for fluids in the fault zone. Geophys. Res. Lett. 24, 1591–1594.

Townend, J., Zoback, M.D., 2000. How faulting keeps the crust strong. Geology 28, 399–402.

Unsworth, M.J., Malin, P., Egbert, G.D., Booker, J.R., 1997. Internal structure of the San Andreas fault at Parkfield, California. Geology 25, 359–362.

Unsworth, M.J., Egbert, G.D., Booker, J.R., 1999. High resolution electromagnetic imaging of the San Andreas fault in Central California. J. Geophys. Res. 104, 1131–1150.

Unsworth, M.J., Bedrosian, P., Eisel, M., Egbert, G., Siripunvaraporn, W., 2000. Along strike variations in the electrical structure of the San Andreas fault at Parkfield, California. Geophys. Res. Lett. 27, 3021–3024.

Waldhauser, F., Ellsworth, W.L., 2000. A double-difference earthquake location algorithm: method and application to the northern Hayward fault. Bull. Seismol. Soc. Am. 90, 1353–1368.

Waldhauser, F., Ellsworth, W.L., 2002. Fault structure and mechanics of the Hayward Fault, California, from double-difference earthquake locations. J. Geophys. 107 (doi: 10.1029/2000JB000084).

Walter, A.W., Mooney, W.D., 1982. Crustal structure of the Diablo and Gabilan ranges, central California: a reinterpretation of existing data. Bull. Seismol. Soc. Amer. 72, 1567–1590.

Wang, C.Y., Rui, F., Zhengsheng, Y., Xingjue, S., 1986. Gravity anomaly and density structure of the San Andreas fault zone. Pure Appl. Geophys. 124, 127–140.

Wiese, H., 1962. Geomagnetische Tiefentellurik Teil: II. die Streichrichtung der Untergrundstrukturen des elektrischen Widerstandes, erschlossen aus geomagnetischen Variationen. Geofis. Pura Appl. 52, 83–103.

Wilson, I.F., 1943. Geology of the San Benito Quadrangle, California. Report of the State Mineralogist of California 39. California Division of Mines and Geology. pp. 183–270.

Zoback, M.D., Zoback, M.L., Mount, V.S., Suppe, J., Eaton, J.P., Healy, J.H., Oppenheimer, D., Reasenberg, P., Jones, L., Raleigh, C.B., Wong, I.G., Scotti, O., Wentworth, C., 1987. New evidence on the state of stress of the San Andreas fault. Science 238, 1105–1111.